(Received 23 June 2025, Accepted 3 September 2025, Scheduled 12 September 2025)

A Novel Conformal Fork-Shaped Antenna for X-Band Wireless Communications

Chilakampalli Anjani, Usha Devi Yalavarthi*, and Boddapati T. P. Madhav

Department of ECE, Koneru Lakshmaiah Education Foundation, AP, India

ABSTRACT: This paper proposes a novel and compact conformal fork-shaped microstrip patch antenna operating at 10.2 GHz for X-band wireless communications. It features a fork shaped unique radiating structure optimized for impedance matching, bandwidth enhancement, and compactness. Parametric studies confirmed optimal performance at feed width 3.5 mm and thickness 0.4 mm. An operating band from 9.31 to 11.88 GHz for $S_{11} <= -10$ dB with a bandwidth of 2.57 GHz is attained. It exhibits a peak gain of 5.6 dB at 10.2 GHz with radiation efficiency 88.29%. To validate its suitability for flexible and modern wireless applications, conformal models are developed, and their performance is analyzed for metrics like operating band, radiation patterns, peak gain, and radiation efficiency. It is prototyped on a Rogers RT Duroid 5880 substrate, and experimental validation demonstrates strong correlation between simulated and measured characteristics.

1. INTRODUCTION

Microstrip patch antennas play a vital role in advanced communication and sensing systems in X-band, serving as critical components for efficient transmission and reception. As the demand for these technologies grows, research continues to focus on developing innovative antenna solutions that meet stringent performance requirements including compact size. The research on antennas for advanced communication and sensing systems in X-band encompasses a wide range of innovative designs tailored for specific applications. Locker et al. [1] presented an efficient low-profile slot antenna designed specifically for X-band applications. Eldek et al. [2] introduced a modified printed bow-tie antenna, capable of single and dual polarization covering both C- and X-bands (5.5–12.5 GHz). Authors in [3] explored a dual-polarized planar array antenna designed for airborne radar operating in both S- and X-bands. A wideband offset slot-coupled patch antenna array suitable for multimode radars in X- and Ku-bands is proposed in [4]. Dastkhosh et al. [5] developed a lightweight, high-gain broadband antenna using a polarization-rotation method specifically tailored for X-band radar systems. Liu et al. [6] designed a flexible coplanar waveguide (CPW)-fed fishtail-shaped antenna optimized for dual-band operations. Shen et al. [7] introduced a novel bidirectional circularly polarized antenna for X-band operation.

Zhao et al. [8] designed a low-profile, broadband, dual-polarized integrated patch subarray specifically intended for synthetic aperture radar (SAR) payloads aboard small satellites. Mao et al. [9] presented a dual-band circularly polarized shared-aperture antenna array capable of simultaneous operation at C- and X-bands. Sarkar et al. [10] reported a defected ground structure (DGS)-integrated, air-loaded wideband microstrip antenna optimized for X- and Ku-band applications. Aboserwal et al. [11] described an ultra-compact dual-polarized slotted waveguide array unit cell developed for large-scale electronic scanning radar systems operating in X-band. Mekimah et al. [12] introduced a broadband, circularly polarized, CPW-fed asymmetric slot patch antenna targeting X-band usage. Leszkowska et al. [13] developed a high-gain circularly polarized superstrate antenna specifically designed for CubeSat applications within X-band frequencies. Jang et al. [14] investigated a high-durability X-band patch antenna with an innovative CPW feeding network. The design was particularly aimed at ensuring durability under harsh conditions such as external shocks, a critical consideration in military and naval radar systems. Zhou et al. [15] proposed a shared-aperture wideband L/X-band phased array antenna designed for synthetic aperture radar (SAR) platforms. Yang et al. [16] designed a cavity-backed dual-polarized wideband antenna for X-band systems. Nunna and Kothapudi [17] introduced a novel conformal linear polarized antenna array sharing a common aperture designed for combined C- and X-band spaceborne SAR systems. Chung et al. [18] discussed the design of a compact dual-band antenna suitable for low-earth-orbit satellites within the Internet of Vehicle (IoV) context. Siragam [19] explored nanocomposite materials for developing a miniaturized, high-bandwidth microstrip patch antenna targeted at X-band applications. The novel substrate significantly improved dielectric characteristics, enhancing overall antenna performance, thus making it suitable for compact wireless devices requiring broadband operation. Chen et al. [20] developed a flexible, wideband X-band antenna array utilizing metasurface technology with reduced radar cross-section (RCS). However, these contributions generally face trade-offs: rigid structures limit flexible inte-

* Corresponding author: Usha Devi Yalavarthi (usha.yalavarthi@kluniversity.in).

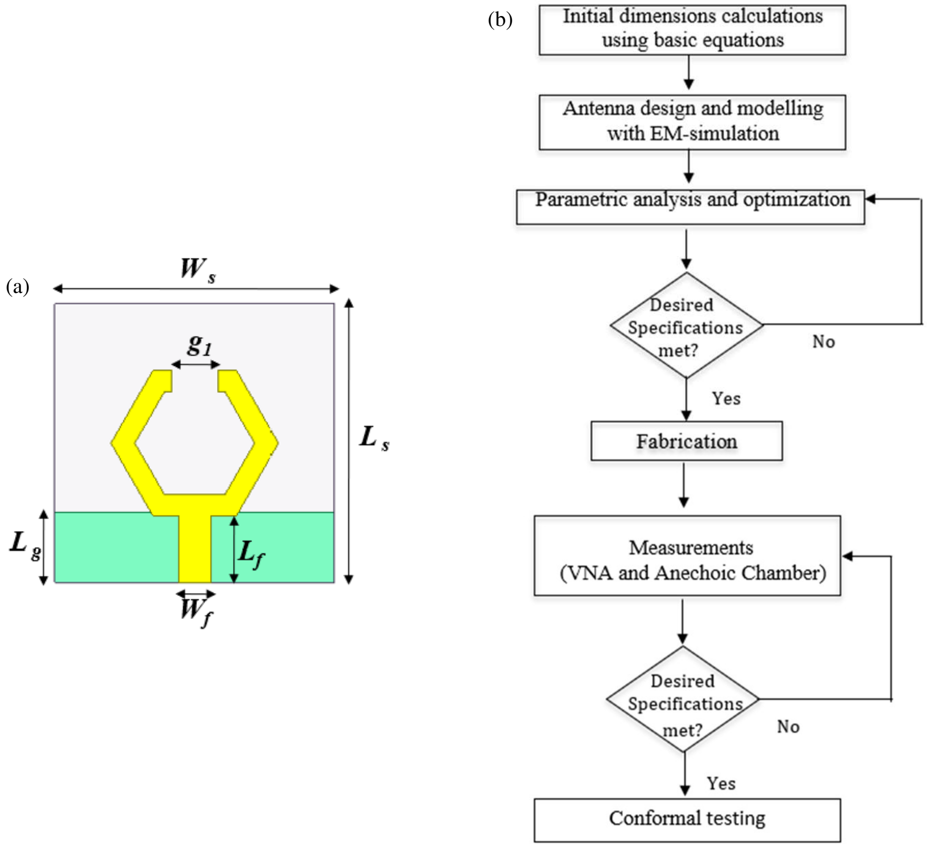

FIGURE 1. (a) Proposed antenna simulation view. (b) Methodology flow chart.

gration; conformal designs often compromise radiation efficiency ($< 85\%$); and miniaturized geometries tend to degrade gain. Despite progress, there remains a lack of compact X-band antennas that simultaneously achieve: high radiation efficiency ($> 85\%$) under conformal bending, balanced performance across gain, bandwidth, and stable electrical behavior across multiple bending angles (10°–90°).

The proposed compact fork-shaped microstrip patch antenna operating at 10.2 GHz is aimed at advanced communication and sensing systems such as radar, satellite communications, and high-speed wireless networks. Antenna design and its parametric analysis are presented in Section 2. Results investigated like S_{11} characteristics, field distributions, and far-field radiation characteristics are described in Section 3. Conformal models of the proposed antenna developed for various bending angles and their analysis are presented in Section 4. Proposed antenna comparison with the existing state-of-art literature is discussed in Section 5, and Section 6 gives the conclusion of proposed work.

The novelty of the proposed antenna lies in three aspects: Geometric novelty: The fork-shaped radiating patch introduces an optimized arm gap g_1 and feed width $W_f = 3.5$ mm, which significantly improves impedance matching and bandwidth without increasing the antenna footprint ($30 \times 30\,\text{mm}^2$). This geometry achieves balanced current distribution and reduced back radiation, which are not simultaneously realized in conventional flat umbrella or capacitively loaded patches. Performance novelty: The combination of a compact footprint, 2.57 GHz impedance bandwidth, peak gain of 5.6 dB, and 88.29% radiation efficiency at 10.2 GHz surpasses many existing designs in the literature, as shown in Table 6, while maintaining structural integrity in conformal configurations. Fabrication novelty: The antenna is fabricated on a Rogers RT duroid 5880 substrate of 0.4 mm thickness using precision milling followed by SMA connector integration. The process ensures consistent geometry for both planar and bent prototypes.

2. ANTENNA DESIGN

Figure 1(a) illustrates novel and compact fork-shaped antenna structure. The structure incorporates a fork-shaped radiating patch situated on a dielectric substrate (Rogers RT Duroid 5880) with an overall dimension of $W_s \times L_s$. The dimensions of proposed antenna are initially calculated using standard microstrip antenna design equations [21, 22] as presented in Equations (1)–(5) to achieve the desired resonant frequency. Feedline dimensions are chosen to match the characteristic impedance of $50\,\Omega$, ensuring efficient power transfer to the radiating element. The modified fork-shaped radiating patch is connected to the feedline of width W_f and length L_f. The gap between the radiating arms, denoted as g_1, is optimized to improve impedance matching and bandwidth. Bottom layer is partial ground plane with length L_g and is designed to ensure

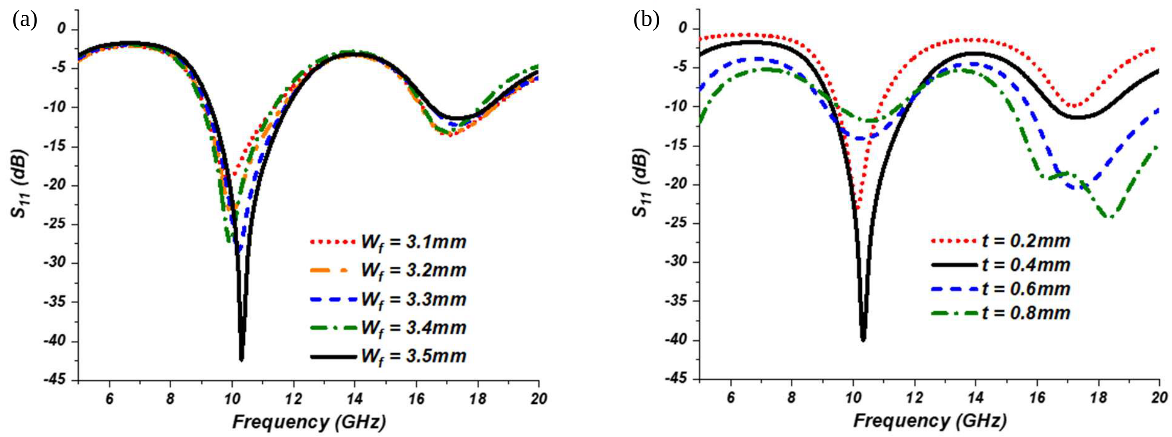

FIGURE 2. Parametric analysis of proposed antenna. (a) With respect to variations in feedwidth. (b) With respect to variations in substrate thickness.

TABLE 1. Design parameters of proposed antenna in mm.

L_s	W_s	L_f	W_f	L_g	g_1
30	30	7.2	3.5	7.5	5

proper reflection and propagation of electromagnetic waves. Finalized dimensions of the proposed antenna geometry are tabulated in Table 1.

The methodology followed is given in following steps and represented in a flowchart (Figure 1(b)):

1. Initial patch dimensions are computed using standard microstrip antenna equations [21, 22] for a target frequency of 10.2 GHz.
2. The fork-shaped structure is modeled, incorporating parameterized feed width 'W_f' and substrate thickness 't'.
3. 'W_f' is varied between 3.1–3.5 mm and 't' between 0.2–0.8 mm to observe S_{11}, bandwidth, and gain trends.
4. Simulation results are iteratively refined to achieve $S_{11} \leq -10$ dB and maximum bandwidth with constraints on compactness and fabrication feasibility.
5. The optimized design is milled on Rogers RT Duroid 5880, cleaned and fitted with an SMA connector.
6. S_{11} is measured using a VNA, and radiation patterns, gain, and efficiency are evaluated in an anechoic chamber.
7. Antenna prototypes are tested under bending angles of 10°, 20°, 30°, 45°, 60°, and 90° to evaluate the stability of electrical characteristics.

The width of microstrip patch w_P is given by:

$$w_P = \frac{c}{2f_r}\sqrt{\frac{2}{\varepsilon_r + 1}} \tag{1}$$

where ε_r is the relative dielectric constant, and f_r is the resonant frequency.

The effective dielectric constant $\varepsilon_{reffect}$ is calculated as:

$$\varepsilon_{reffect} = \frac{\varepsilon_r + 1}{2} + \frac{\varepsilon_r - 1}{2}\left[\left(1 + \frac{12t}{w_p}\right)^{-\frac{1}{2}} + 0.04\left(1 - \frac{w_P}{t}\right)^2\right] \tag{2}$$

The length of microstrip patch L_p is given by:

$$L_p = \left\{\frac{c}{2f_r\sqrt{\varepsilon_{reffect}}}\right\} \tag{3}$$

Input impedance Z_{in} and width of microstrip feed line W_f are related as:

$$Z_{in} = \frac{60}{\sqrt{\varepsilon_{reffect}}}\ln\left(\frac{8t}{W_f} + \frac{W_f}{4t}\right); \text{ for } \frac{W_f}{t} < 1 \tag{4}$$

$$Z_{in} = \frac{120\pi}{\sqrt{\varepsilon_{reffect}}\left[\frac{W_f}{t} + 1.393 + \frac{2}{3}\ln\left(\frac{W_f}{t} + 1.444\right)\right]}; \quad \text{for } \frac{W_f}{t} > 1 \tag{5}$$

where t is the thickness of substrate.

To optimize the proposed antenna performance, parametric analysis with respect to feedline width (W_f) and substrate thickness (t) are performed, and the S_{11} characteristics are represented in Figures 2(a) and (b). W_f variation is shown in Figure 2(a), and it is varied from 3.1 mm to 3.5 mm. As W_f increases, the impedance matching improves, leading to a significant reduction in S_{11} at the resonant frequency. The best performance is achieved for $W_f = 3.5$ mm, where S_{11} reaches its minimum value indicating optimal power transfer and reduced reflection losses. The impact of 't' variations is depicted in Figure 2(b), and 't' ranges from 0.2 mm to 0.8 mm. It is evident that increasing the substrate thickness shifts the resonant frequency slightly and alters the magnitude of S_{11}. A thicker substrate enhances bandwidth but may also introduce additional fringing effects, slightly detuning the resonance. The optimal

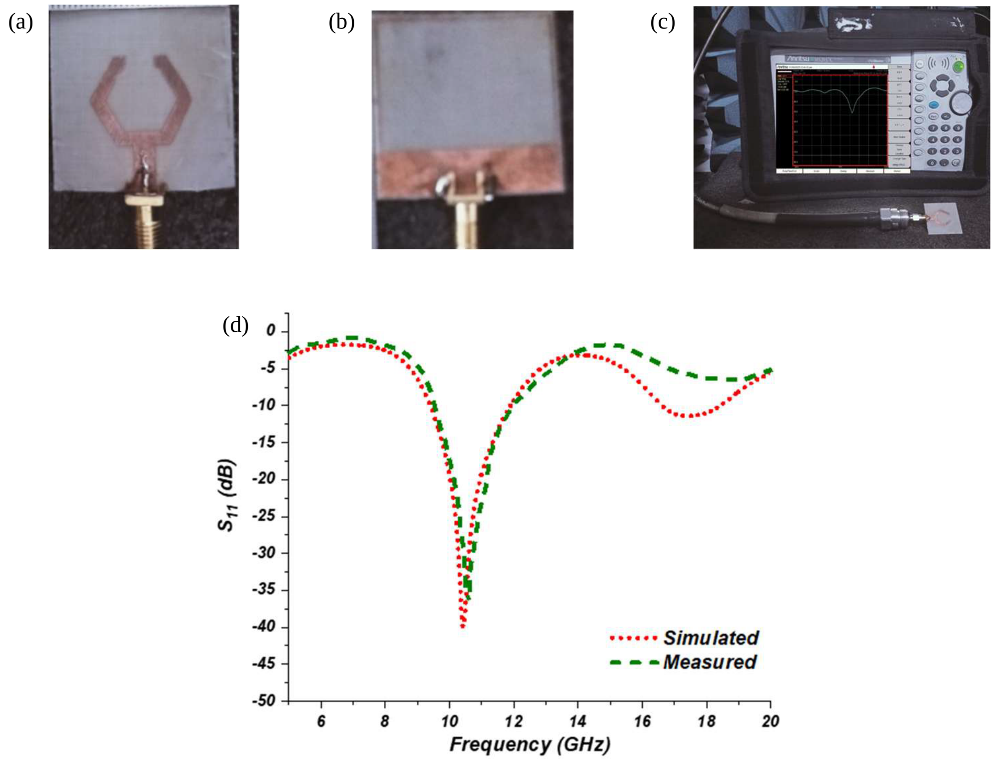

FIGURE 3. Prototype model and S_{11} characteristics. (a) Top view. (b) Bottom view. (c) Measurement setup on VNA. (d) S_{11} characteristics.

TABLE 2. S_{11} values in parametric analysis w.r.t W_f.

W_f (mm)	Operating Band (GHz)	Bandwidth (GHz)
3.1	9.06–11.35	2.29
3.2	9.14–11.65	2.51
3.3	9.17 – 11.72	2.55
3.4	9.08–11.36	2.28
3.5	9.31–11.88	2.57

TABLE 3. S_{11} values in parametric analysis w.r.t 't'.

t (mm)	Operating Band (GHz)	Bandwidth (GHz)
0.2	9.48–10.85	1.37
0.4	9.31–11.88	2.57
0.6	9.15–11.69	2.54
0.8	9.56–11.43	1.87

thickness $t = 0.4$ mm offers a balanced trade-off among compactness, bandwidth enhancement, and minimized reflection losses.

From a manufacturing perspective, dimensional variations are inevitable in mass production, especially in feed width (W_f) and substrate thickness (t). The parametric analysis shown in Figures 2(a) and 2(b) indicates that small deviations in W_f (± 0.1 mm) and t (± 0.2 mm) cause only slight shifts in the resonant frequency and minimal changes in bandwidth. This tolerance resilience implies that the proposed design can be reliably fabricated using standard printed circuit board (PCB) or flexible substrate manufacturing processes without significant performance degradation, making it suitable for large-scale production. Table 2 and Table 3 give operating bands and bandwidth of the proposed antenna for parametric analysis w.r.t 'W_f' and 't' respectively.

3. RESULTS AND DISCUSSIONS

3.1. Impedance Bandwidth

Figure 3(a) depicts the top view of fabricated antenna, and Figure 3(b) presents the bottom view showing the ground plane configuration and the soldered connector for interfacing. Figure 3(c) illustrates the experimental setup on Vector Network Analyzer (VNA) to measure S_{11} characteristics. Figure 3(d) compares measured and simulated S_{11} characteristics of the proposed antenna. It operates from 9.31 to 11.88 GHz for $S_{11} <= -10$ dB with a bandwidth of 2.57 GHz. From Figure 3(d), measured and simulated values are in fine agreement.

3.2. Current, E and H Field Distributions

Field distributions of the proposed antenna at 10.2 GHz resonant frequency are analyzed to provide insights into its radiation characteristics. These distributions include surface current (Jsurf), electric field (E-field), and magnetic field (H-field) as shown in Figures 4(a), (b), and (c), respectively. Surface current distribution from Figure 4(a) highlights regions of maximum current intensity across the radiating structure. The current is predominantly concentrated around the edges of feedline and central section of fork-shaped patch. This indicates strong coupling and effective radiation from these areas. The symmetry of the current distribution further confirms a balanced energy flow leading to efficient antenna performance.

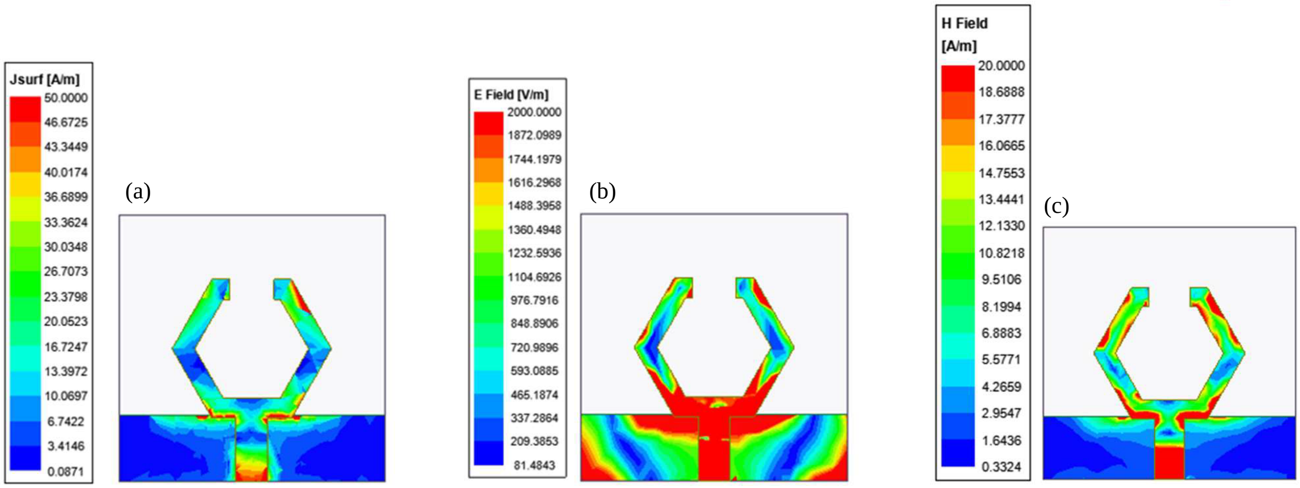

FIGURE 4. Field distributions of the proposed antenna at 10.2 GHz. (a) Surface current distribution. (b) E-field distribution. (c) H-field distribution.

In Figure 4(b), E-field distribution reveals areas of the highest electric field intensity. The strongest fields are observed at inner edges of the fork-shaped patch and near feedline connection, demonstrating that these regions are critical for energy radiation. H-field distribution in Figure 4(c) complements E-field, showing the regions of magnetic energy concentration. The magnetic field intensity is most pronounced around the junction between feedline and radiating patch.

3.3. Far-Filed Radiation Characteristics

The 3D gain plot of proposed antenna at resonant frequency of 10.2 GHz is depicted in Figure 5. The maximum gain is observed to be 5.6 dB which is achieved at main lobe, indicating a strong and focused radiation pattern. The side lobes are minimal, and the back radiation is significantly suppressed, ensuring reduced interference and improved performance. Figures 6(a) and (b) represent simulated and measured radiation patterns at 10.2 GHz in E- and H-planes. In E-plane patterns, Figure 6(a), simulated and measured co-polarization patterns show good agreement, exhibiting a clear directive radiation characteristic. The cross-polarization levels remain significantly lower, indicating excellent polarization purity. The E-plane shows strong co-polarization agreement, while cross-polarization remains at least 20 dB lower, confirming polarization purity suitable for satellite and radar links. In the H-plane (Figure 6(b)), minor deviations are observed between simulated and measured side lobes. These differences are attributed to fabrication tolerances (± 0.1 mm in feed width) as well as connector soldering and chamber reflections.

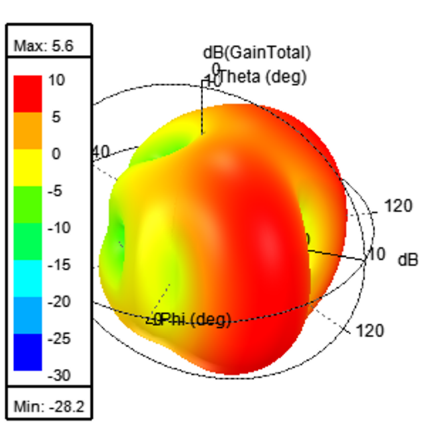

FIGURE 5. 3D gain plot at 10.2 GHz.

The measured radiation patterns directly impact system-level performance in X-band applications such as radar, satellite links, and high-speed wireless networks. The gain G is related to directivity D and radiation efficiency η by Equations (6) and (7):

$$G(\theta, \phi) = \eta D(\theta, \phi) \tag{6}$$

where,

$$D_{\max} = \frac{4\pi U_{\max}}{P_{rad}} \tag{7}$$

For practical estimation, the main-lobe beamwidths determine the approximate directivity given in Equation (8):

$$D_{approx} \approx \frac{41,253}{HPBW_E \times HPBW_H} \tag{8}$$

where $HPBW_E$ and $HPBW_H$ are half power beamwidth values in E- and H-planes, respectively.

At 10.2 GHz, the measured half-power bandwidth (HPBW) values in the E- and H-planes correspond to a directivity consistent with the observed peak gain (5.6 dB) given an efficiency of $\sim 88\%$. The observed low side-lobe levels (< -15 dB) reduce interference and improve angular resolution in radar applications. Cross-polarization levels being > 20 dB lower than co-polarization ensure minimal polarization mismatch loss, critical for maintaining link reliability in satellite communications.

Peak gain characteristics of the proposed antenna are illustrated in Figure 7. Minor discrepancies between simulation and measurement are observed which may be attributed to fabrication tolerances or measurement conditions. The antenna achieved the maximum peak gain of 5.65 dB at 9.9 GHz, and

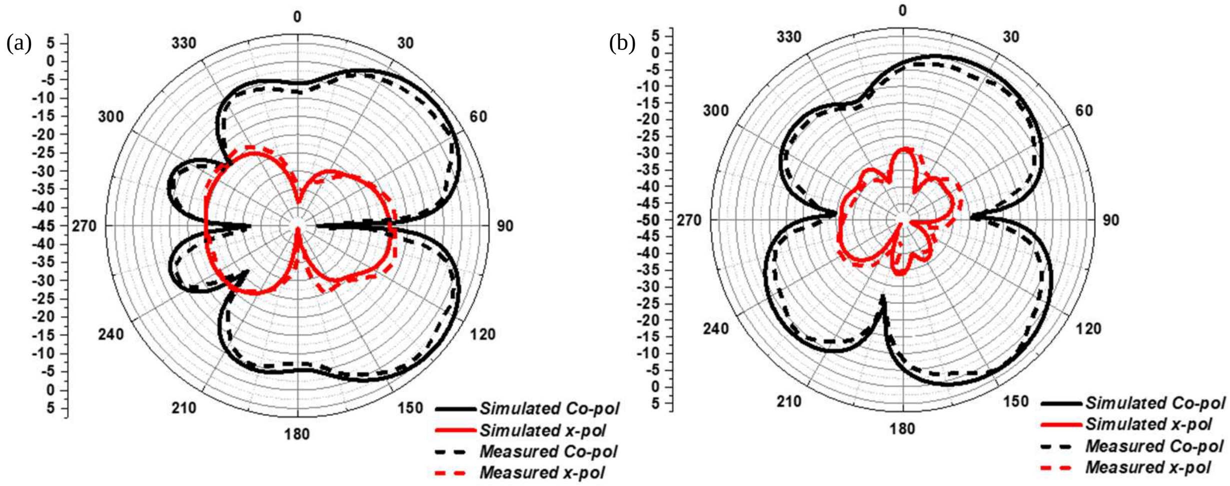

FIGURE 6. Radiation patterns at 10.2 GHz. (a) E-plane. (b) H-plane.

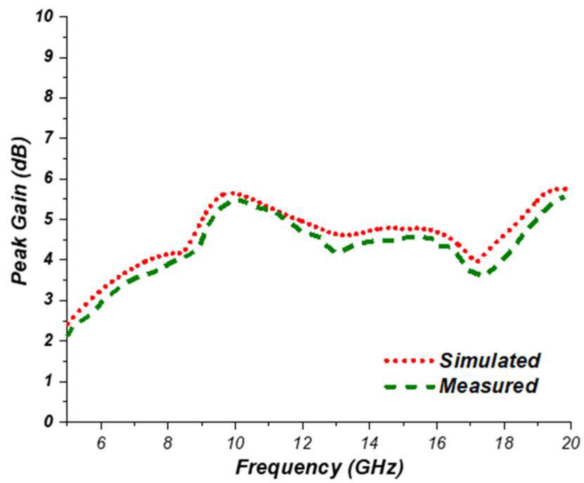

FIGURE 7. Peak gain characteristics.

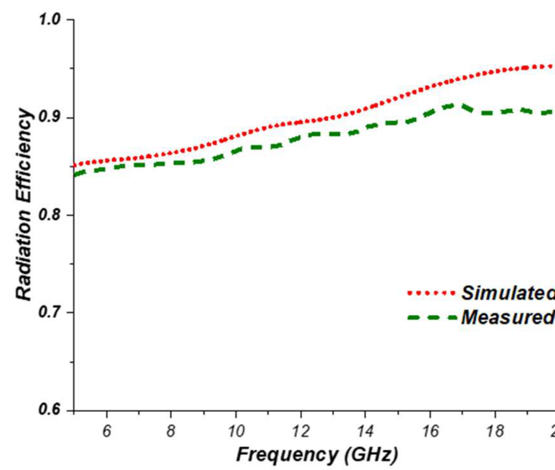

FIGURE 8. Radiation efficiency characteristics.

at 10.2 GHz frequency the peak gain is 5.60 dB. Radiation efficiency characteristics are depicted in Figure 8. Both simulated and measured efficiencies remain consistently high exceeding 83% across the entire frequency range. At 10.2 GHz frequency, radiation efficiency is 88.29%, and simulation results exhibit slightly higher efficiency than the measured values particularly at higher frequencies. This variation could be due to additional losses during the experimental setup.

4. CONFORMAL MODELS AND ANALYSIS

To validate the conformability of proposed antenna model, conformal models are developed subjected to varying bending angles, ranging from 10° to 90° as presented in Figure 9. The geometry of proposed antenna is analyzed under these deformation scenarios to evaluate its performance in non-planar configurations. At smaller bending angles, such as 10° and 20°, the structural deformation is minimal preserving the overall shape and symmetry of the antenna. As the bending angle increases to 30° and 45°, the curvature becomes more pronounced, potentially affecting its impedance matching and radiation properties. For higher bending angles such as 60° and 90°, the structure undergoes significant distortion that may induce changes in electromagnetic field distribution. These models are crucial for understandingthe proposed antenna performance under practical applications where conformal integration with curved surfaces is required. Figure 10 illustrates the flexible bending prototype model of proposed antenna.

Figure 11 presents S_{11} characteristics of conformal antenna models across various bending angles ranging from 10° to 90°. The graph shows that the proposed antenna maintains a satisfactory impedance matching across the frequency range with S_{11} values remaining below -10 dB, which is a standard benchmark for effective radiation performance. At smaller bending angles such as 10° and 20°, S_{11} performance is consistent with minimal deviation, indicating a negligible effect of curvature. As the bending angles increase to 30°, 45°, 60°, and 90°, slight variations in the resonance frequency and reflection coefficient are observed. However, the proposed antenna continues to exhibit acceptable performance, demonstrating its robustness and adaptability to conformal surfaces. Operating bands of conformal model for various bending angles are tabulated in Table 4.

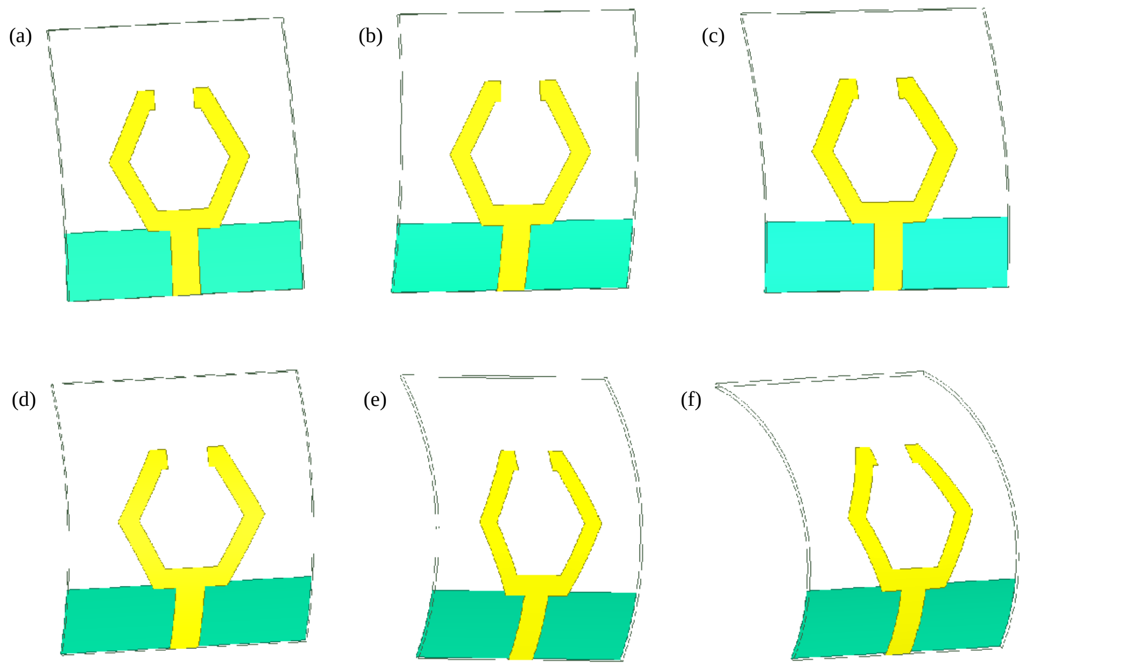

FIGURE 9. Conformal models at various bending angles. (a) 10 deg, (b) 20 deg, (c) 30 deg, (d) 45 deg, (e) 60 deg, (f) 90 deg.

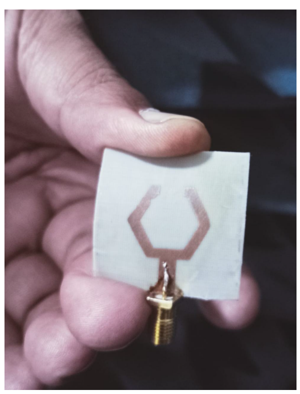

FIGURE 10. Proposed antenna flexible bending.

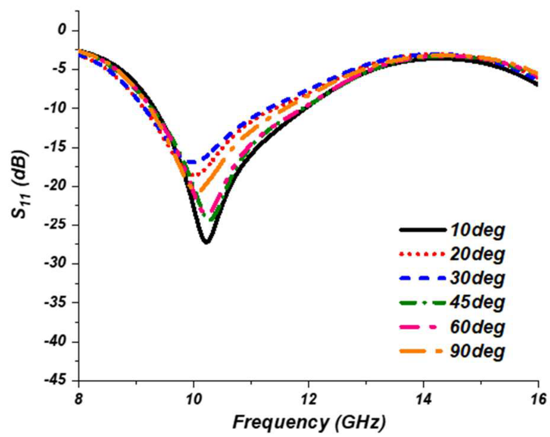

FIGURE 11. S_{11} characteristics of conformal models.

TABLE 4. Operating bands of conformal models.

Conformal model	Operating band (GHz)	Bandwidth (GHz)
10°	9.35–11.92	2.57
20°	9.16–11.41	2.25
30°	9.05–11.22	2.17
45°	9.29–11.87	2.58
60°	9.27–11.85	2.58
90°	9.23–11.59	2.36

Figure 12 presents the radiation patterns of conformal antenna models at 10.2 GHz for various bending angles. Figures 12(a) and (b) illustrate the E-plane and H-plane patterns for bending angles of 10°, 20°, and 30°. In E-plane, the co-polarized radiation exhibits a directional main lobe with side lobes which remain consistent across all three angles, with minimal variations in gain and beamwidth. H-plane patterns maintain the shape and alignment of main lobe, but slight deviations in side-lobe levels are observed due to the increase in curvature. Figures 12(c) and (d) present radiation patterns for higher bending angles of 45°, 60°, and 90°. E-plane patterns in Figure 12(c) maintain well-defined main-lobe and side-lobe stable directional patterns whereas H-plane patterns in Figure 12(d) demonstrate consistent alignment of radiation characteristics with small variations in side-lobe levels as the curvature increases.

Figure 13 illustrates peak gain characteristics of conformal antenna models at various bending angles across a frequency range of 8–16 GHz. Figure 13(a) presents the gain performance for bending angles of 10°, 20°, and 30°. The results indicate that peak gain remains relatively stable across the frequency range with minimal variations as the bending angle increases. Figure 13(b) presents the gain behaviour for higher bending an-

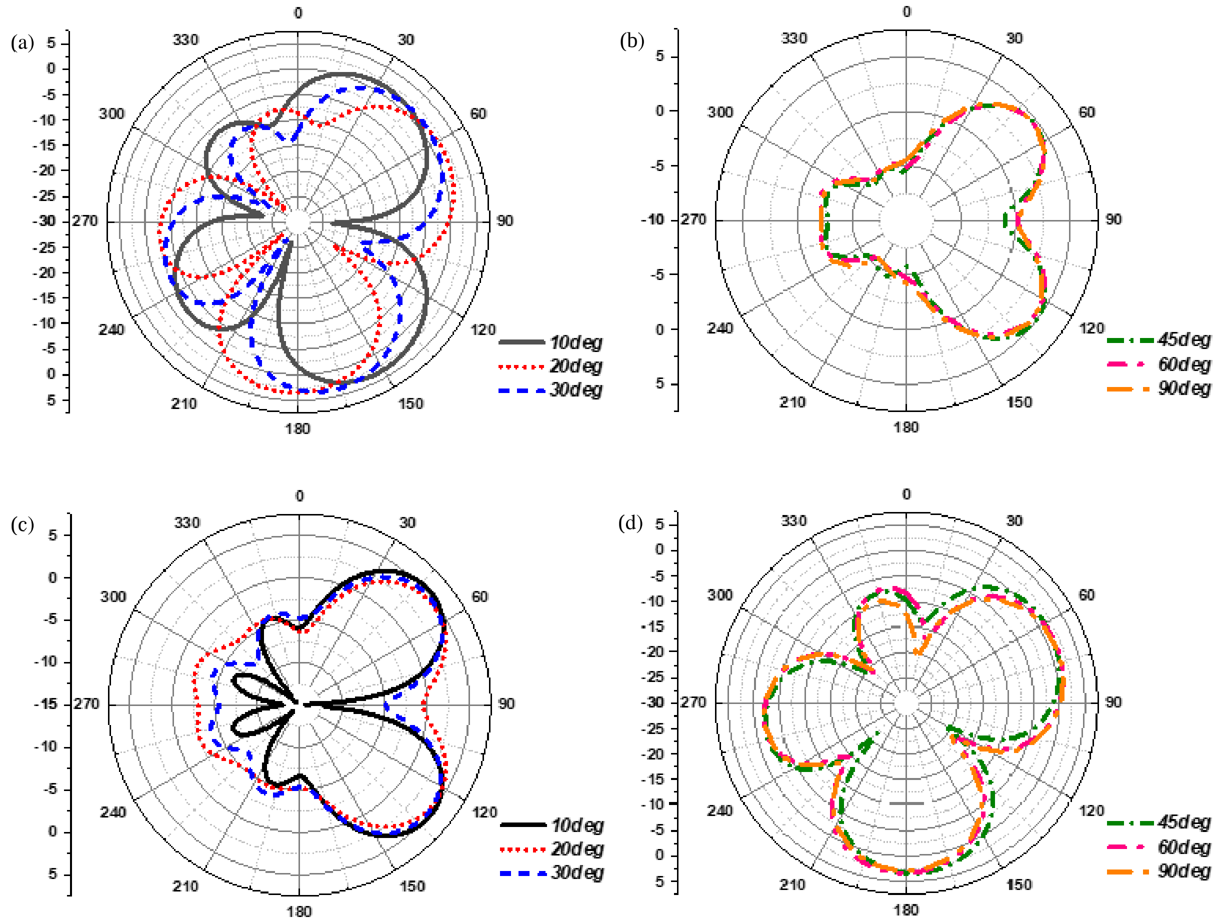

FIGURE 12. Radiation patterns of conformal models at 10.2 GHz. (a) E-plane for 10, 20 and 30 deg. (b) H-plane for 10, 20 and 30 deg. (c) E-plane for 45, 60 and 90 deg. (d) H-plane for 45, 60 and 90 deg.

gles of 45°, 60°, and 90°. A slight reduction in gain is observed at extreme bending angles particularly near the upper end of the frequency range. This can be due to increased deformation, which may slightly alter the antenna radiation characteristics.

Figure 14 illustrates radiation efficiency characteristics of conformal antenna models. Figure 14(a) depicts the efficiency for bending angles of 10°, 20°, and 30°, and Figure 14(b) shows the efficiency for larger bending angles of 45°, 60°, and 90°. The results demonstrate consistently high efficiency exceeding 83% throughout the frequency range, with minimal variations across different angles. Peak gain and radiation efficiency values of conformal models for various bending angles are tabulated in Table 5. The conformal bending study (10°–90°) demonstrates that resonance shifts are minimal (< 150 MHz), and S_{11} remains < -10 dB across all cases. As bending increases, a slight redistribution of surface currents induces small variations in impedance matching. Importantly, efficiency remains above 83% throughout, indicating the limited coupling between mechanical strain and electrical degradation. This resilience suggests that the proposed antenna is well suited for flexible aerospace and wearable platforms where structural curvature is inevitable.

TABLE 5. Peak gain values of conformal models at 10.2 GHz.

Conformal model	Peak gain (dB)	Radiation efficiency (%)
10°	5.55	84.07
20°	5.60	85.23
30°	5.60	84.91
45°	5.67	84.98
60°	5.73	85.21
90°	5.68	84.33

5. COMPARISON

Proposed antenna performance is presented in relevance with other recent research works on X-band microstrip patch antennas in Table 6. Parameters that are considered for comparison are operating band, bandwidth, and gain. Table 6 shows that the proposed model excels in radiation efficiency and maintains a favourable balance between bandwidth and gain, particularly when its conformal capability is considered. While some designs in literature achieve marginally higher gain, they do so at the expense of efficiency, footprint, or flexibility. The proposed model optimizes these parameters for balanced performance in practical X-band applications.

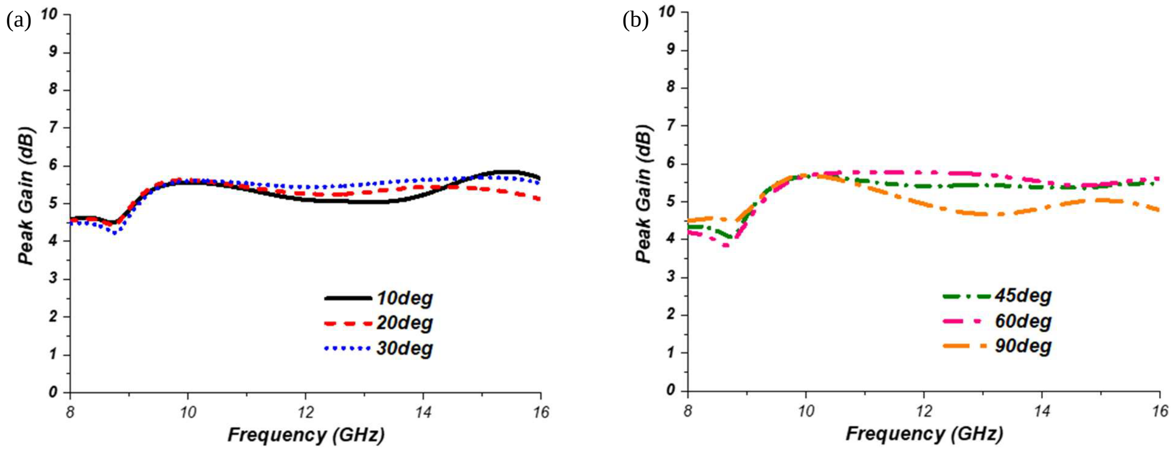

FIGURE 13. Peak gain characteristics of conformal models. (a) 10, 20 and 30 deg. (b) 45, 60 and 90 deg.

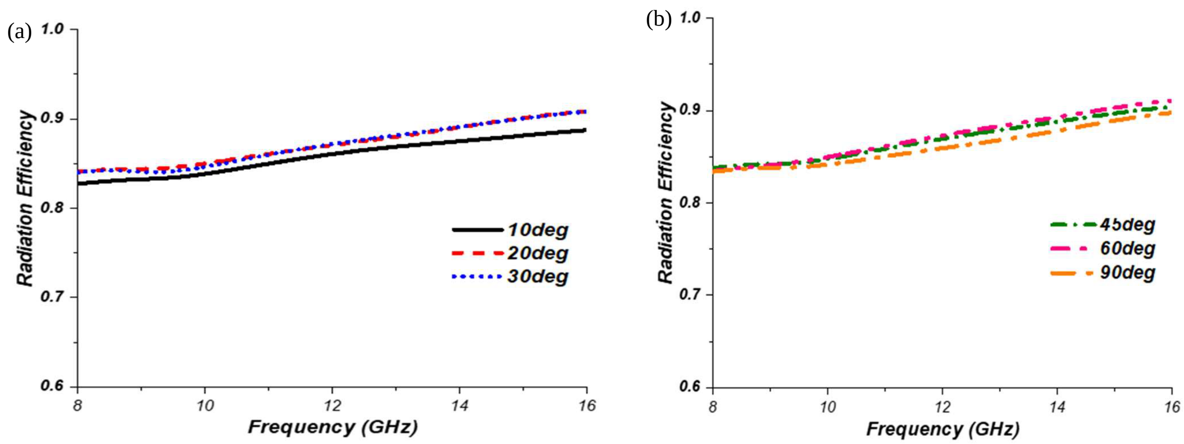

FIGURE 14. Radiation efficiency characteristics of conformal models. (a) 10, 20 and 30 deg. (b) 45, 60 and 90 deg.

TABLE 6. Comparison of proposed antenna with relevant works.

Ref. No.	Type of Antenna (Structure)	Antenna Dimensions (mm^3)	Operating Band (GHz)	Bandwidth (GHz)	Gain (dB)	Radiation Efficiency (%)
[7]	Bidirectional antenna with asymmetrical Y-shaped feed	20 × 16 × 0.5	X-band (∼ 8 GHz band)	4	4.60	80.00
[12]	CPW-fed asymmetrical slot patch antenna	24 × 22 × 0.25	7–10.2	3.2	4.00	85.00
[16]	Cavity-backed dual-polarized patch antenna	13.2 × 13.2 × 11.7	X-band (8–12 GHz)	4	4.50–5.80	68.00
[18]	Dual-band slot antenna (inverted triangle and U-shaped slot)	30 × 13 × 0.254	10.87–12.76, 15.19–16.02	1.89, 0.83	3.34–6.08, 3.50–4.65	80.80
Proposed Antenna	Compact fork-shaped microstrip patch antenna	30 × 30 × 0.4	9.31–11.88	2.57	5.60	88.29

6. CONCLUSION

The proposed novel and compact conformal fork-shaped antenna achieved high-performance metrics at the target frequency of 10.2 GHz for X-band applications. It is designed and fabricated on Rogers RT Duroid 5880 of thickness 0.4 mm for flexibility. It obtained an impedance bandwidth of 2.57 GHz ($S_{11} <= -10$ dB) operating in X-band. Parametric analysis is performed to optimize the performance of antenna. It obtained 5.6 dB peak gain at 10.2 GHz with 88.29% radiation efficiency. Conformal models for various bending angles of 10°, 20°, 30°, 45°, 60°, and 90° are developed and analyzed for the conformal performance of proposed antenna. The fabricated antenna demonstrates strong agreement with simulations. The measured resonance shift was < 120 MHz ($\sim 1.1\%$), gain deviation < 0.2 dB, and efficiency variation $< 5\%$. It also maintained performance under conformal bending conditions that demonstrates its versatility for applications requiring flexible or curved surface integration.

ACKNOWLEDGEMENT

Authors would like to acknowledge the DST through technical support from SR/PURSE/2023/196 and SR/FST/ET-II/2019/450.

REFERENCES

[1] Locker, C., T. Vaupel, and T. F. Eibert, "Radiation efficient unidirectional low-profile slot antenna elements for X-band application," *IEEE Transactions on Antennas and Propagation*, Vol. 53, No. 8, 2765–2768, Aug. 2005.

[2] Eldek, A. A., A. Z. Elsherbeni, and C. E. Smith, "Wide-band modified printed bow-tie antenna with single and dual polarization for C- and X-band applications," *IEEE Transactions on Antennas and Propagation*, Vol. 53, No. 9, 3067–3072, Sep. 2005.

[3] Hsu, S.-H., Y.-J. Ren, and K. Chang, "A dual-polarized planar-array antenna for S-band and X-band airborne applications," *IEEE Antennas and Propagation Magazine*, Vol. 51, No. 4, 70–78, Aug. 2009.

[4] Bilgic, M. M. and K. Yegin, "Wideband offset slot-coupled patch antenna array for X/Ku-band multimode radars," *IEEE Antennas and Wireless Propagation Letters*, Vol. 13, 157–160, 2014.

[5] Dastkhosh, A. R., H. D. Oskouei, and G. Khademevatan, "Compact low weight high gain broadband antenna by polarization-rotation technique for X-band radar," *International Journal of Antennas and Propagation*, Vol. 2014, No. 1, 743046, 2014.

[6] Liu, H., S. Zhu, P. Wen, X. Xiao, W. Che, and X. Guan, "Flexible CPW-fed fishtail-shaped antenna for dual-band applications," *IEEE Antennas and Wireless Propagation Letters*, Vol. 13, 770–773, 2014.

[7] Shen, J., C. Lu, W. Cao, J. Yang, and M. Li, "A novel bidirectional antenna with broadband circularly polarized radiation in X-band," *IEEE Antennas and Wireless Propagation Letters*, Vol. 13, 7–10, 2013.

[8] Zhao, X., B. N. Tian, S. P. Yeo, and L. C. Ong, "Low-profile broadband dual-polarized integrated patch subarray for X-band synthetic aperture radar payload on small satellite," *IEEE Antennas and Wireless Propagation Letters*, Vol. 16, 1735–1738, 2017.

[9] Mao, C.-X., S. Gao, Y. Wang, Q.-X. Chu, and X.-X. Yang, "Dual-band circularly polarized shared-aperture array for C-/X-band satellite communications," *IEEE Transactions on Antennas and Propagation*, Vol. 65, No. 10, 5171–5178, Oct. 2017.

[10] Sarkar, T., A. Ghosh, L. L. K. Singh, S. Chattopadhyay, and C.-Y.-D. Sim, "DGS-integrated air-loaded wideband microstrip antenna for X- and Ku-band," *IEEE Antennas and Wireless Propagation Letters*, Vol. 19, No. 1, 114–118, Jan. 2020.

[11] Aboserwal, N., J. L. Salazar-Cerreno, and Z. Qamar, "An ultra-compact X-band dual-polarized slotted waveguide array unit cell for large E-scanning radar systems," *IEEE Access*, Vol. 8, 210 651–210 662, 2020.

[12] Mekimah, B., T. Djerafi, A. Messai, and A. Belhedri, "Broadband circularly polarized CPW-fed asymmetrically-shaped slot patch antenna for X band applications," *Progress In Electromagnetics Research Letters*, Vol. 91, 137–143, 2020.

[13] Leszkowska, L., M. Rzymowski, K. Nyka, and L. Kulas, "High-gain compact circularly polarized X-band superstrate antenna for CubeSat applications," *IEEE Antennas and Wireless Propagation Letters*, Vol. 20, No. 11, 2090–2094, Nov. 2021.

[14] Jang, D., T. H. Lim, D. Kim, S. Wang, and H. Choo, "Design of a high-durability X-band patch antenna with a CPW feeding network based on a durability evaluation analysis," *Electronics*, Vol. 11, No. 4, 553, Feb. 2022.

[15] Zhou, W.-L., S.-W. Qu, M. Xia, and S. Yang, "Wideband L/X-band shared-aperture phased array antenna for SAR applications," *IEEE Transactions on Antennas and Propagation*, Vol. 70, No. 11, 10 475–10 484, 2022.

[16] Yang, Y.-H., B.-Y. Liu, and S.-G. Zhou, "A wideband cavity-backed dual-polarized antenna for X-band applications," *IEEE Antennas and Wireless Propagation Letters*, Vol. 22, No. 4, 913–917, 2022.

[17] Nunna, B. A. and V. K. Kothapudi, "A novel C/X-band linear polarized conformal shared aperture antenna array for spaceborne SAR applications," *IEEE Access*, Vol. 11, 101 045–101 054, 2023.

[18] Chung, M.-A., K.-C. Tseng, and I.-P. Meiy, "Antennas in the internet of vehicles: Application for X band and Ku band in low-earth-orbiting satellites," *Vehicles*, Vol. 5, No. 1, 55–74, Jan. 2023.

[19] Siragam, S., "Nanocomposite marvels: Miniaturized high bandwidth microstrip patch antenna for X-band applications," *Next Materials*, Vol. 5, 100243, 2024.

[20] Chen, H., Q. Zhen, J. Chen, H. Sun, H. Li, L. F. Chernogor, Z. Sun, Y. Zheng, T. Liu, and Z. Jin, "X-band and low-RCS flexible wideband antenna array based on metasurface," *IEEE Antennas and Wireless Propagation Letters*, Vol. 24, No. 3, 567–571, Mar. 2025.

[21] Balanis, C. A., *Antenna Theory: Analysis and Design*, 3rd ed., John Wiley & Sons, New Jersey, 2005.

[22] Kraus, J. D., R. J. Marhefka, and A. S. Khan, *Antennas and Wave Propagation*, 4th ed., Mc-Graw Hill, 2005.